International Journal of Applied Earth Observation and Geoinformation 125 (2023) 103581

Contents lists available at ScienceDirect

International Journal of Applied Earth Observation and Geoinformation

journal homepage: www.elsevier.com/locate/jag

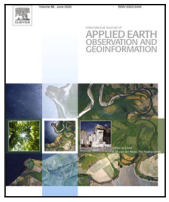

Analysis of the performance of polarimetric PSI over distributed scatterers with Sentinel-1 data☆

Jiayin Luo [a], Juan M. Lopez-Sanchez [a,*], Francesco De Zan [b]

[a] Institute for Computer Research (IUII), University of Alicante, Alicante, E-03080, Spain
[b] delta phi remote sensing GmbH, Gilching, 82205, Germany

ARTICLE INFO

Keywords:
Sentinel−1
Polarimetry
Interferometry
Distributed scatterer
Deformation

ABSTRACT

Sentinel−1 (S1) data enables effective monitoring of displacements using persistent scatterer interferometry (PSI). S1 includes VV and VH polarization channels, allowing us to apply polarimetric techniques to PSI. In short, polarimetric PSI (PolPSI) exploits the available polarization channels to enhance the identification and processing of measurement points including persistent scatterers (PS) and distributed scatterers (DS). Previous works have shown the benefits of using PolPSI for PS points with S1 data, but the corresponding analysis for DS is missing.

DS points are processed by finding a neighborhood of statistically homogeneous pixels (SHP) and averaging the phase within that neighborhood. In this work we show how dual-polarimetric data are stricter on the selection of the SHP group than single-polarimetric data. Thanks to the information added by the second channel, different land covers are not mixed in the SHP group. As a result, the number of points in the SHP groups is generally smaller than with VV alone, but they are more reliable. The impact of this strategy on the resulting deformation estimates is also investigated in this work, showing that the deformation areas are fully preserved and the influence of nearby pixels associated with other scene elements is avoided.

1. Introduction

Persistent Scatterer Interferometry (PSI) is an important technique for monitoring ground deformation. It exploits interferogram stacks created from a time series of satellite Synthetic Aperture Radar (SAR) images (Ferretti et al., 2000, 2001; Berardino et al., 2002; Hooper et al., 2004, 2007; Rosi et al., 2016). This technique largely relies on identifying pixels with consistently stable phase over time, for example, buildings and infrastructures, which are defined as persistent scatterers (PS). In addition to PS, advanced PSI approaches also incorporate distributed scatterers (DS), located in roads, rural areas, etc., and which require a special processing to derive the deformation measurements (Ferretti et al., 2011; Wang et al., 2023). The joint use of PS and DS enhances the capabilities of PSI techniques, allowing for comprehensive ground deformation monitoring in heterogeneous scenarios (Dong et al., 2021).

The launch of polarimetric SAR (PolSAR)-equipped satellites, like TerraSAR−X, Radarsat−2, Sentinel−1 (S1), ALOS−PALSAR, ALOS2−PALSAR2, and, more recently, COSMO−SkyMed−2, SAOCOM, and LT−1, makes it feasible to collect consistent time series of polarimetric images. In the last years, particular emphasis has been placed on S1, a constellation of two C-band SAR satellites, which offers VV and VH images with a short revisit time (6 or 12 days) and under a free and open access policy. With the available polarimetric data sets, it is possible to explore the potential benefits of utilizing the additional channels provided by these satellites to improve the results of PSI. With this objective, polarimetric PSI (PolPSI) algorithms were proposed, aimed at investigating how the integration of the polarimetric information could lead to improvements concerning accuracy, reliability, and spatial density of the measurement points (Navarro-Sanchez and Lopez-Sanchez, 2012; Luo et al., 2022).

In PolPSI, the available polarimetric channels are combined into an optimized one. This process is carried out for optimizing a cost function associated with the pixel quality and used as a selection criterion. With a common goal of providing a stable phase measure, the amplitude dispersion index is chosen as the primary selection criterion for

☆ This work was supported in part by the European Funds for Regional Development and by the Spanish Ministry of Science and Innovation (Agencia Estatal de Investigación, AEI) with Project PID2020-117303GB-C22/AEI/10.13039/501100011033, and in part by the Generalitat Valenciana, Conselleria de Innovacion, Universidades, Ciencia y Sociedad Digital with Project CIAICO/2021/335. The research was also partially performed in the ESA-MOST China DRAGON-5 project ref. 59339.

* Corresponding author.
E-mail address: juanma.lopez@ua.es (J.M. Lopez-Sanchez).

https://doi.org/10.1016/j.jag.2023.103581
Received 26 June 2023; Received in revised form 5 November 2023; Accepted 18 November 2023
Available online 22 November 2023

PSI (Navarro-Sanchez et al., 2010; Zhao and Mallorqui, 2019a; Iglesias et al., 2015), whereas coherence is commonly used for distributed scatterer interferometry (DSI) (Pipia et al., 2009; Navarro-Sanchez and Lopez-Sanchez, 2012; Iglesias et al., 2014). For amplitude dispersion, the deformation computation is straightforwardly performed using the optimized channel. In contrast, in DSI the computation of coherence necessitates an additional step before the PolPSI optimization, which is the spatial filtering of the interferograms. Currently, efforts to enhance PolPSI technology primarily focus on two key areas. First, different adaptive spatial filtering strategies and specific processing workflows for DSI have been proposed (Navarro-Sanchez and Lopez-Sanchez, 2014; Mullissa et al., 2017, 2018; Zhao et al., 2022; Shen et al., 2022a,b). Second, researchers are working to make the processing quicker and more effective (in terms of both PSI and DSI), as seen in the work by Zhao et al. (2023).

The adaptive filtering in DSI requires identification of similar pixels surrounding the reference point, for which several approaches have been proposed (Parizzi and Brcic, 2011). The Kolmogorov–Smirnov (KS) test (Stephens, 1970) was employed in DespecKS technique by Ferretti et al. (2011) (SqueeSAR^{TM}), which exploits the time series of the amplitude of the SAR images. The generalized likelihood ratio (GLR) test can be used with amplitude data (Deledalle et al., 2015), interferometric data (Dong et al., 2018), polarimetric data (Luo et al., 2023), and polarimetric and interferometric data (Deledalle et al., 2015). Other approaches have been proposed in Sica et al. (2018, 2021), Murdaca et al. (2022). Apart from the statistical properties employed in these approaches, Mullissa et al. (2017, 2018) and Zhao and Mallorqui (2019b) estimated the similarity between pixels based on scattering mechanisms. In all cases, polarimetric or not, the pixels similar to a reference one are called the statistically homogeneous pixels (SHP). Once the SHP set of each pixel has been identified, the interferograms are computed by averaging over the SHPs. Most PolPSI studies with DS (Navarro-Sanchez and Lopez-Sanchez, 2014; Mullissa et al., 2018; Shen et al., 2022b; Zhao et al., 2022) have been focused on the number of measurement points reached, showing an increase when polarimetric data are used with respect to single-pol data, thanks to the optimization provided by polarimetry, in any of its forms. Such an optimization entails an improved quality of the selected pixels with respect to single-pol data.

However, despite the demonstrated contribution of PolPSI to PSs and DSs, the common practice in most companies and services providing ground deformation measurements from S1 data, e.g. the European Ground Motion Service, consists of discarding the VH channel from the beginning and computing the deformation products based on the VV channel alone. In the case of PS, we recently studied the physical origin of the advantage of PolPSI for S1 data (Luo et al., 2022). We found that the VH channel provided two different contributions: a stable response over time in many urban locations in which the VV channel exhibited fluctuations, and a stronger response in scene pixels dominated by scatterers rotated with respect to the incidence plane. As a result, the optimized channel for PS outperformed the VV channel. Such a study focused on the roots of the difference between single-pol and dual-pol data has not been carried out for DS yet. In this work, we aim at assessing the physical origin of the contribution of PolPSI to DSI processing. Our purpose is to highlight the problems associated with the use of VV alone, and how PolPSI helps avoid them.

In summary, with the focus on S1 data, we aim to answer the following questions:

1. What is the contribution of using dual-polarimetric data in the SHP group identification, from the point of view of the scene properties?
2. Is there a quantitative improvement in the final results in terms of number of DS and/or quality of the estimated deformation?
3. Is it worth to use always the VH channel, in addition to VV, or is it better to work with the VV channel alone?

To carry out this analysis we have made use of the GLR test as the SHP selection criterion because it offers a common framework for both single-pol and dual-pol data. In the same vein, we have exploited the basic Coherent Pixels Technique (CPT) (Mora et al., 2003; Blanco-Sanchez et al., 2009) for the deformation estimation. It is important to clarify that more advanced techniques, especially designed for polarimetric DSI, such as those proposed by Mullissa et al. (2018) or Shen et al. (2022a), could provide better final results, but the main conclusions regarding the advantages of dual-pol data over single-pol data would remain unaltered. Consequently, a comparison of polarimetric DSI techniques is also beyond the scope of this work.

2. Formulation

Each acquisition of S1 consists of a pair of VV and VH images. To prepare the collection of S1 data gathered over the research area during the selected period, a series of preprocessing steps were performed using the ESA SNAP software[1] (Luo et al., 2022). After obtaining the stack of coregistered images, the PolPSI algorithm can be applied. The processing steps are shown in Fig. 1.

2.1. Polarimetric optimization

A target vector $\boldsymbol{k}$ is used for representing each pixel in S1 images as

$$\boldsymbol{k} = \left[S^{VV}, S^{VH}\right]^T \tag{1}$$

where S^{VV} and S^{VH} stands for the vertical co-polar and cross-polar channel, respectively. T is the transpose operator. To facilitate the projection of each vector $\boldsymbol{k}$ onto a scalar μ, a complex column vector $\boldsymbol{\omega}$ is employed (Cloude and Papathanassiou, 1998). This projection allows the fusion of the two polarimetric channels into a new channel denoted as,

$$\mu = \boldsymbol{\omega}^{*T}\boldsymbol{k} \tag{2}$$

where $*$ represents the conjugate operator, and $\boldsymbol{\omega}$ is identical across all images within one dataset under the equal scattering mechanism (ESM) (Neumann et al., 2008) constraint.

The polarimetric optimization consists of finding the projection vector that optimizes the selection criterion. This task can be carried out using an exhaustive search on the available polarimetric space (Navarro-Sanchez and Lopez-Sanchez, 2014), but it can be very demanding from the computational viewpoint. As a more efficient alternative, we adopted the SNR-based (Signal-to-Noise Ratio) method (Wu et al., 2015, 2016) to define the optimum projection vector $\boldsymbol{\omega}$:

$$\boldsymbol{\omega}^{*T} = \frac{1}{\sqrt{1+{x_1}^2}}\left[1, x_1 e^{j\theta_1}\right] \quad \begin{cases} x_1 \in [0,\infty) \\ \theta_1 \in [-\pi,+\pi) \end{cases} \tag{3}$$

in which both x_1 and θ_1 are real numbers. This method offers a reduced computational burden by conducting two sequential one-dimensional searches. The next step involves determining the optimal parameters x_1 and θ_1 within $\boldsymbol{\omega}$. This parameter selection process is typically guided by two widely adopted criteria: minimizing the amplitude dispersion index D_A for PS points or maximizing the average interferometric coherence $\overline{|\gamma|}$ for DS points. In practice, the search grids of x_1 and θ_1 for both D_A and $\overline{|\gamma|}$ optimizations are set as $[-\pi, -2/3\pi, -1/3\pi, 0, 1/3\pi, 2/3\pi, \pi]$ and $[2^0, 2^2, 2^4, 2^6, \ldots, 2^{16}]$, respectively.

The calculation of D_A is performed using all single look complex (SLC) images directly,

$$D_A = \frac{\sigma_a}{\bar{a}} = \frac{1}{\overline{|\boldsymbol{\omega}^{*T}\boldsymbol{k}|}\sqrt{N-1}}\sqrt{\sum_{i=1}^{N}(|\boldsymbol{\omega}^{*T}\boldsymbol{k}_i| - \overline{|\boldsymbol{\omega}^{*T}\boldsymbol{k}|})^2} \tag{4}$$

[1] https://step.esa.int/main/toolboxes/snap/

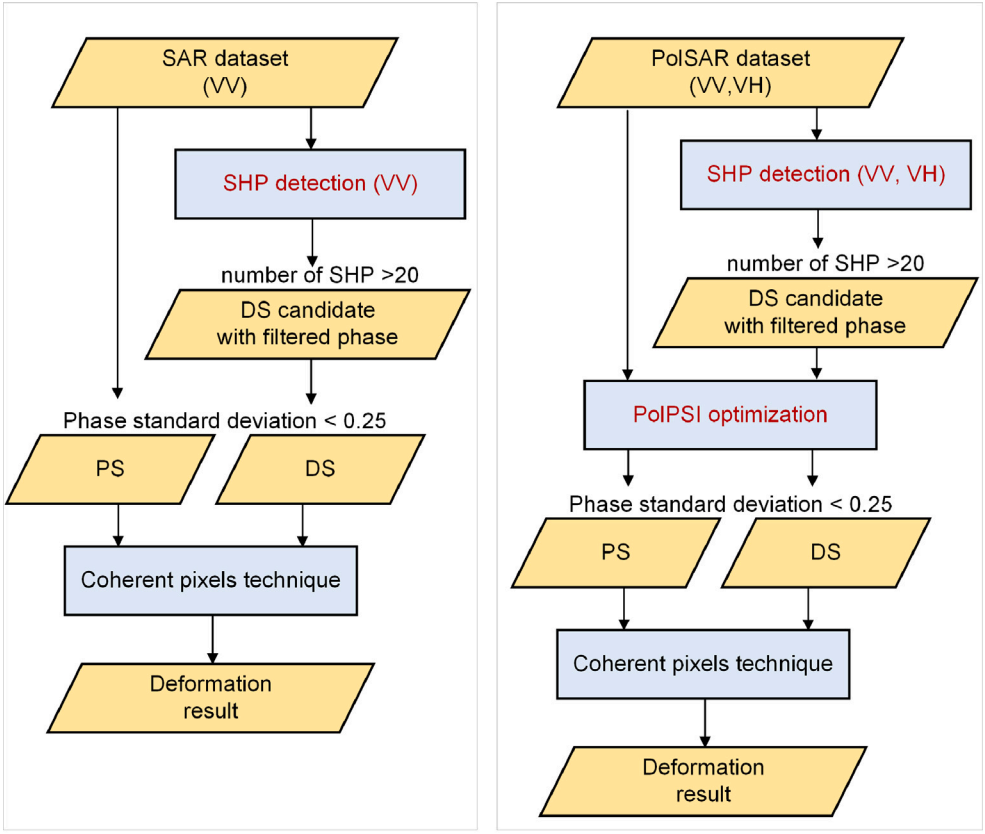

Fig. 1. Processing flowcharts. (a) PSI for VV (or VH) channel; (b) PolPSI for VV and VH channels. The differing steps are marked in red. The SHP detection is based on GLR test with false alarm rate = 5%. The search window is defined as 15 × 15 pixels. (For interpretation of the references to color in this figure legend, the reader is referred to the web version of this article.)

where σ_A and $\bar{a}$ are the standard deviation and the mean value of image amplitude, respectively. N is the number of images in the time series, and the overline indicates the empirical mean value.

The average interferometric coherence $\overline{|\gamma|}$ is computed based on multi-look interferograms. The multi-look process within the spatial neighborhood is employed to reduce the effect of speckle, which will weaken the properties of the PS but improve the phase quality of DS. For each pixel, the multi-look covariance matrices in each interferogram are computed as,

$$\boldsymbol{C}_{ii} = E\left[\boldsymbol{k}_i \boldsymbol{k}_i^{*T}\right], \boldsymbol{C}_{jj} = E\left[\boldsymbol{k}_j \boldsymbol{k}_j^{*T}\right], \boldsymbol{\Omega}_{ij} = E\left[\boldsymbol{k}_i \boldsymbol{k}_j^{*T}\right] \tag{5}$$

where E is the expectation operator computed by spatial averaging pixels in the SHP set, and $\boldsymbol{k}_i$ and $\boldsymbol{k}_j$ represent images acquired at different dates. $\overline{|\gamma|}$ is defined based on multi-look covariance matrices and projection vector $\boldsymbol{\omega}$:

$$\overline{|\gamma|} = \frac{1}{K}\sum_{k=1}^{K}|\gamma_k|, \quad \text{with } \gamma_k(\boldsymbol{\omega}) = \frac{\boldsymbol{\omega}^{*T}\boldsymbol{\Omega}_{ij}\boldsymbol{\omega}}{\sqrt{\boldsymbol{\omega}^{*T}\boldsymbol{C}_{ii}\boldsymbol{\omega}}\sqrt{\boldsymbol{\omega}^{*T}\boldsymbol{C}_{jj}\boldsymbol{\omega}}} \tag{6}$$

where K is the number of selected interferograms.

2.2. Adaptive filtering based on SHP detection

As illustrated in Fig. 1, before the processing of DS, images are adaptively filtered based on the SHP. SHP were detected by evaluating pixel similarity within the spatial neighborhood using the GLR test. The reason for choosing GLR test is that it can be applied conveniently to both single-polarization or multi-polarization data using the same principle and a well founded mathematical criterion for threshold selection. The similarity between pixels is measured based on the temporal average of the covariance matrix,

$$\boldsymbol{C} = \frac{1}{N}\sum_{i=1}^{N}\boldsymbol{k}_i\boldsymbol{k}_i^{*T} \tag{7}$$

When dual-polarization data are employed, the dimension m of matrix $\boldsymbol{C}$ is equal to 2. In the case of single polarization data, $\boldsymbol{C}$ becomes the intensity of VV or VH. As a result, m reduces to 1.

If the number of looks p fulfills $p \geq m$, the multi-look covariance matrix obtained from (7) follows a complex Wishart distribution,

$$p(\boldsymbol{C}|\boldsymbol{\Sigma}) = \frac{|\boldsymbol{C}|^{p-m}}{K(p,m)|\boldsymbol{\Sigma}|^{p}}\exp(-\mathrm{tr}(\boldsymbol{\Sigma}^{-1}\boldsymbol{C})) \tag{8}$$

where $K(p,m) = \pi^{m(m-1)/2}\prod_{k=1}^{m}\Gamma(p-k+1)$, $\Gamma()$ represents the Gamma function (Goodman, 1963).

The task of assessing the similarity between $\boldsymbol{C}_1 \in \mathbf{W}_C(m,p,\boldsymbol{\Sigma})$ and $\boldsymbol{C}_2 \in \mathbf{W}_C(m,p,\boldsymbol{\Sigma})$ (independent and identically distributed with the same covariance matrix $\boldsymbol{\Sigma}$ and multi-looking samples p), can be formulated as a hypothesis test.

$$\begin{aligned} H_0 &: \boldsymbol{\Sigma}_1 = \boldsymbol{\Sigma}_2 \\ H_1 &: \boldsymbol{\Sigma}_1 \neq \boldsymbol{\Sigma}_2 \end{aligned} \tag{9}$$

The criterion Q, which is designed for the above hypothesis test (Conradsen et al., 2003), is expressed as in (10). Higher values of Q indicate higher likelihood of $\boldsymbol{C}_1$ and $\boldsymbol{C}_2$ sharing a common distribution.

$$Q = \frac{(2p)^{2mp}}{p^{2mp}}\frac{|\boldsymbol{C}_1\boldsymbol{C}_2|^{p}}{|\boldsymbol{C}_1+\boldsymbol{C}_2|^{2p}} \tag{10}$$

We quantify the probability of observing a smaller value of $-2\rho \ln Q$ as follows:

$$P(-2\rho \ln Q \le z) = P(\chi^2(m^2) \le z) \tag{11}$$

where $\chi^2()$ is the chi-square distribution function, and $\rho = 1 - (2m^2 - 1)/2pm$.

The determination of the SHP group for the reference pixel is based on,

$$w = \begin{cases} 1, & \text{if } -2\rho \ln Q \le R_{thr} \\ 0, & \text{if } -2\rho \ln Q > R_{thr} \end{cases} \tag{12}$$

where parameter w quantifies the similarity between the reference pixel and the neighborhood pixels with the predefined threshold R_{thr}. The value of R_{thr} is determined by consulting the chi-square distribution table, taking into account the degrees of freedom m^2 and the desired false alarm rate or significance level α. In this context, we have chosen $\alpha = 5\%$. For the dual-pol case, m^2 equals 4, while for a single-pol channel, m^2 equals 1. Consequently, consulting the chi-square table reveals that for dual-pol (optimum channel) and single-pol (VV or VH), R_{thr} equals 9.48 and 3.84, respectively.

Ultimately, the filtered matrices $\hat{\boldsymbol{C}}_{ii}$, $\hat{\boldsymbol{C}}_{jj}$, and $\hat{\boldsymbol{\Omega}}_{ij}$ for each interferogram are computed by performing multi-looking over the corresponding SHP set Ω at the reference pixel.

$$\hat{\boldsymbol{C}}_{ii} = \frac{1}{L} \sum_{\Omega} \boldsymbol{k}_i \boldsymbol{k}_i^{*T} \tag{13}$$

where L is the number of pixels in the SHP set Ω.

2.3. Joint processing of PS and DS

The phase standard deviation σ_ϕ was chosen to define a common selection for jointly processing PS and DS (Navarro-Sanchez and Lopez-Sanchez, 2014). Pixels with σ_ϕ lower than an established threshold 0.25 will be selected as PS or DS.

For PS points, we directly consider the relationship between D_A and σ_ϕ as (Ferretti et al., 2001)

$$\sigma_\phi \approx D_A \tag{14}$$

While for DS points, we define two cases based on the number of independent samples L_e, which can be obtained as a function of the number of pixels in the SHP set L, as

$$L_e \approx \frac{L}{(\text{ovs}_{\text{range}}) \cdot (\text{ovs}_{\text{azimuth}})} \tag{15}$$

where $\text{ovs}_{\text{range}}$ and $\text{ovs}_{\text{azimuth}}$ are the oversampling factors in range and azimuth direction, respectively. For S1 data, $\text{ovs}_{\text{range}} \approx 1.60$, $\text{ovs}_{\text{azimuth}} \approx 1.17$.

1. For $L_e > 10$, σ_ϕ can be approximated as (Hagberg et al., 1995)

$$\sigma_\phi \approx \frac{1}{\sqrt{2N}} \frac{\sqrt{1 - |\gamma|^2}}{|\gamma|} \tag{16}$$

2. A more accurate σ_ϕ is estimated in the case of lower L_e values through a lookup table based on Lee et al. (1994),

$$\sigma_\phi = \sqrt{\int_\phi (\phi - \phi_0)^2 \text{pdf}(\phi) d\phi} \tag{17}$$

with

$$\begin{aligned} \text{pdf}(\phi) = & \frac{\Gamma(L_e + 1/2)(1 - |\gamma|^2)^{L_e} \gamma \cos(\phi - \phi_0)}{2\sqrt{\pi}\Gamma(L_e)(1 - |\gamma|^2 \cos^2(\phi - \phi_0))^{L_e + 1/2}} \\ & + \frac{(1 - |\gamma|^2)}{2\pi} F_1\left(L_e, 1; \frac{1}{2}; \gamma^2 \cos^2(\phi - \phi_0)\right) \end{aligned} \tag{18}$$

where F_1 is the Gauss hypergeometric function, and ϕ_0 was set to zero.

It is worth to note that as the number of SHP increases, the coherence threshold for classifying a point as a DS decreases, since it is considered more reliable.

2.4. Ground deformation estimation

The deformation results are obtained by exploiting the phase of the differential interferogram set. For single polarization images, the interferograms are calculated through the original SLC images acquired at dates i and j,

$$\boldsymbol{I} = S_i^{VV} S_j^{VV*T} \tag{19}$$

For dual polarization data, the interferograms result from an optimized combination of two available SLC images through

$$\boldsymbol{I} = \mu_i \mu_j^{*T} \tag{20}$$

In this study, we utilized the Coherent Pixels Technique (CPT) (Mora et al., 2003; Blanco-Sanchez et al., 2009) for the selection of interferograms and for the deformation estimation. The PSI analysis was conducted using the same algorithm for both single and dual-polarization cases.

3. Data set

The first study area consists of 39 S1 images acquired between April 2017 and August 2018 over the Xiaolangdi Dam in Henan province, China. The dam has a maximum height of 154 m, a crest length of 1667 m, and a width of 15 m. Considering the potential impact of water level and precipitation on the central region of the Xiaolangdi Dam, large deformation could arise (Liu et al., 2021). As a result, a specific test area measuring 141 × 343 pixels around the dam center was chosen. Under this scenario, in-situ data between March 2017 and October 2020 is available as reported in He et al. (2022). He et al. (2022) also employed the S1 dataset to deduce that the dam center experiences deformation at a rate of 20–25 mm/year based on SBAS-InSAR method (Berardino et al., 2002). Furthermore, in a related study by Zhao et al. (2022), the PolPSI method was applied to joint analysis PS and DS with S1 images, but different SHP detection methods were used.

The second area of interest utilizes 189 dual-polarization S1 images acquired from December 2016 to January 2021 over the airport of Barcelona, Spain. The PSI processing method is applied on an excerpt of 341 × 1486 pixels. The T1 terminal of the airport was inaugurated in 2009, together with new access roads. Since then, this terminal and part of the roads have exhibited ground deformation, as reported in several studies (Monserrat et al., 2011; Iglesias et al., 2014). The presence of ground deformation has also been captured through the application of PolPSI techniques in previous works (Navarro-Sanchez and Lopez-Sanchez, 2014; Zhao and Mallorqui, 2019b), so this test site constitutes a good benchmark for comparing the performance of PS and DS measured with dual-pol S1 data over an extended area with man-made targets.

Fig. 2 illustrates the location of study areas, while Table 1 provides the key characteristics of the two data sets.

4. Results

4.1. Selection of PS and DS

In this section, we first focus on comparing the selected PS and DS in the two test areas. For each area, we analyze the results obtained in two different cases: single-pol data (VV or VH channel) and dual-pol data (VV and VH channels). The single-pol channel is directly processed using the PSI method, while in the dual-pol case the data are processed using the PolPSI optimization method, so the resulting channel is referred to as the optimized (OPT) channel.

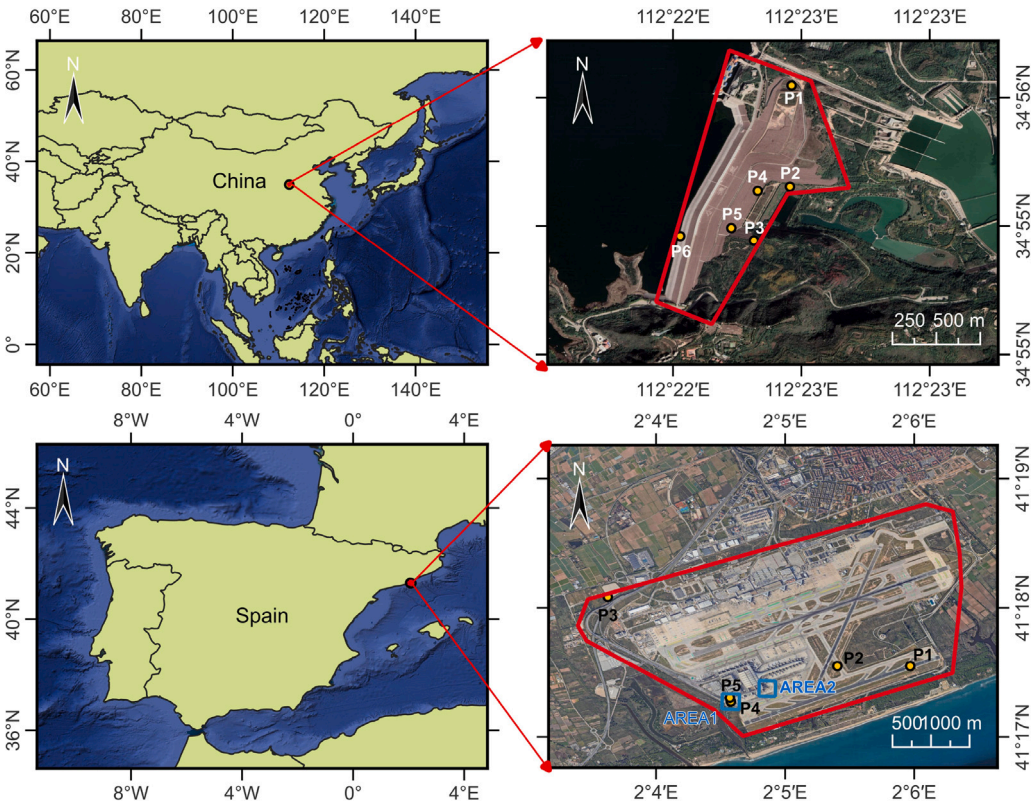

Fig. 2. Location and Google Earth optical image of the test sites. Upper: Xiaolangdi Dam in China. Lower: Barcelona Airport in Spain. The red polygon denotes the S1 subimage processed in this study. The location of pixels and areas in Figs. 5, 6, 7, 12 and 13 are marked here. (For interpretation of the references to color in this figure legend, the reader is referred to the web version of this article.)

Table 1
Key features of the S1 data sets.

Research area	Xiaolangdi dam	Barcelona airport
Acquisition mode	Interferometric Wide-Swath	
Polarization	Dual-pol (VV and VH)	
Pixel spacing (azimuth × range)	13.90 m × 2.33 m	
Orbit	Ascending	
Images	39	189
Time span (start)	04/2017	12/2016
Time span (end)	08/2018	01/2021
Interferograms	411	4200

Table 2
Percentage and number of selected PS and DS for different channels: VV, VH and OPT.

	PS number (percentage)	DS number (percentage)	Total number (percentage)
Test site	Xiaolangdi Dam		
VV	1267 (2.61%)	7026 (14.52%)	8293 (17.13%)
VH	114 (0.23%)	3810 (7.88%)	3924 (8.11%)
OPT	1982 (4.09%)	1680 (3.47%)	3662 (7.46%)
Test site	Barcelona Airport		
VV	4356 (0.85%)	27938 (5.51%)	32294 (6.36%)
VH	3065 (0.60%)	8821 (1.74%)	11886 (2.33%)
OPT	8888 (1.75%)	4403 (0.87%)	13291 (2.62%)

Table 2 shows the percentage and the number of detected PS and DS points in each research area. The values clearly indicate the effectiveness of the PolPSI method in increasing the number of PS points. In the case of the Xiaolangdi Dam, there is an approximate 57% increase compared to the VV channel. It is unsurprising that the VH channel, which has a low amplitude, results in a relatively small number of selected PS points. Notably, for the Barcelona airport, the OPT channel shows an increase of 105% in PS over the VV channel. It is important to note that the physical reasons of the improvement in PS number and quality with dual-pol S1 data with respect to single-pol data were critically analyzed by Luo et al. (2022), therefore we do not repeat that study in this work, which focuses on DS points.

On the other hand, there is an extreme reduction in the number of DS points in both test areas when considering the OPT channel with respect to single-pol data (VV or VH). This confirms the expected impact of incorporating the second channel, since the augmented polarimetric information leads to a stricter selection of DS points. The DS number of the VH channel falls between that of VV and OPT.

To conduct further analysis, the spatial distribution of both PS and DS is presented in Figs. 3 and 4 for Xiaolangdi and Barcelona, respectively.

In Fig. 3(d) and (e), the DS points at VV and VH channel exhibit a widespread distribution across the entire area, covering the main dam as well as the surrounding vegetation areas. There are also DS points along the white rock edge of the dam adjacent to the water. As for the PS points detected by the VV channel they are concentrated in the bare ground area (Fig. 3(a)). Fig. 3(c) reveals the increase in PS obtained at the OPT channel, extending the coverage to a built area at the top of the dam in which the VV channel did not identify PS points. Fig. 3(f) illustrates that DS points are only detected in a small area of the dam. In this case, the pixels on the white rock area adjacent to the water are not selected as DS. This aspect will be further discussed in the next sections.

For the Barcelona airport case in Fig. 4, the DS points found in the OPT channel are located mainly within the runway, while PS points are concentrated in nearby residential and industrial areas, roads and airport buildings. The VV channel exhibits a lower density of PS and

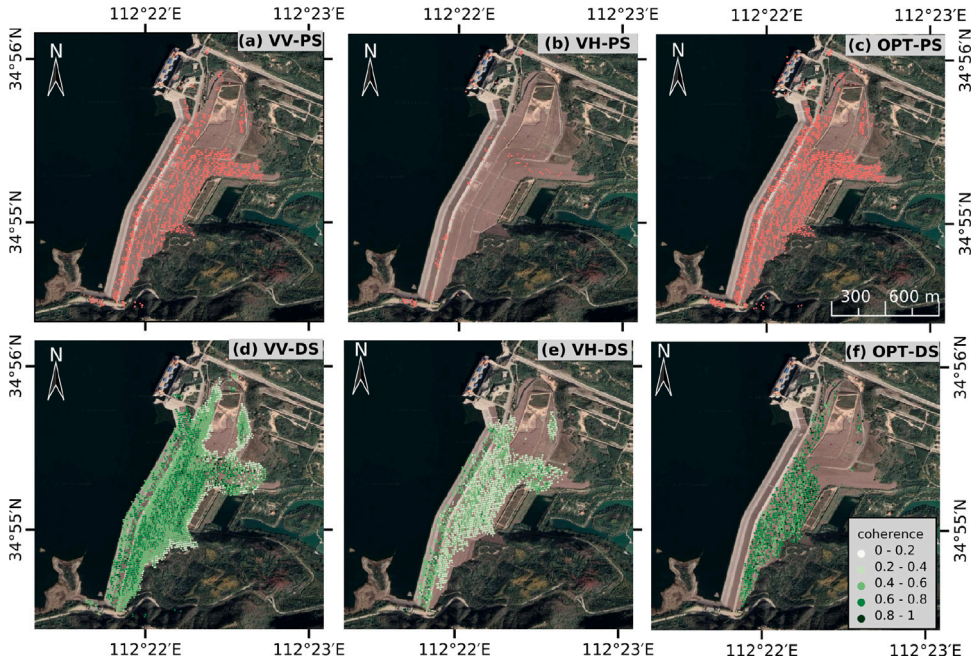

Fig. 3. Distribution of PS (a)–(c) and DS (d)–(f) over Xiaolangdi Dam. For DS points, the coherence value is shown.

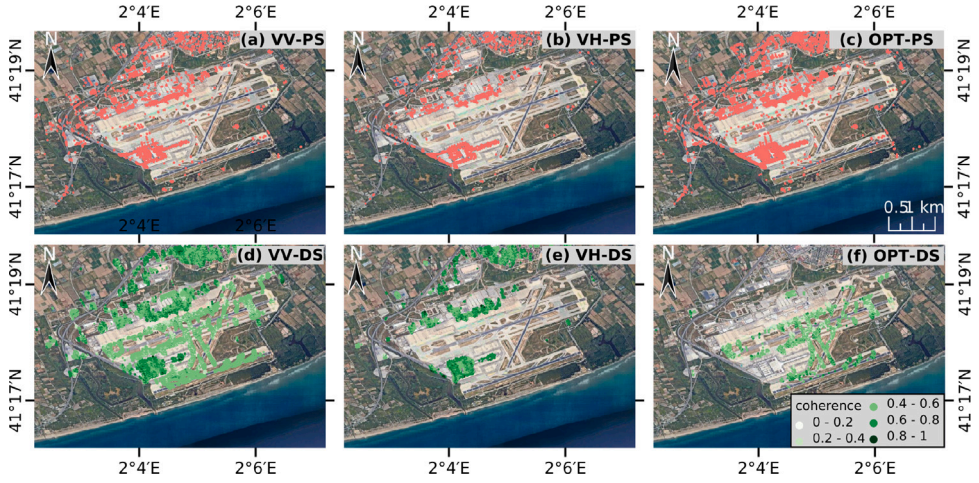

Fig. 4. Distribution of PS (a)–(c) and DS (d)–(f) over Barcelona Airport. For DS points, the coherence value is shown.

a higher number of DS compared to the OPT channel. The VH is unable to identify DS located on the runway due to its low amplitude value, which leads to reduced coherence in this channel. As observed in Fig. 4(d), the increase in DS contributes to a notably increased coverage of measurement points. The distribution of DS in VV channel extends beyond the runway and includes man-made structures. Both VV and VH channel selects many points as DS in the airport buildings. Nevertheless, these points were expected to be PS, based on their physical properties.

4.2. Analysis of the quality of the DS points

Although the VV channel exhibits an increase in DS points, the reliability of these points still needs to be discussed. Firstly, coherence maps of the DS found at VV, VH and OPT channel were generated, which are shown in Fig. 3(d)–(f) and Fig. 4(d)–(f) for Xiaolangdi Dam and Barcelona Airport, respectively. As illustrated in Fig. 3(d), the coherence values in the borders of the areas covered by DS points consistently fall below 0.4, since they usually include vegetation at the boundaries of the dam zone. From the definition of σ_ϕ, these pixels were selected mainly due to the higher number of similar pixels determined through the GLR test.

The central area corresponds to bare ground and rocks, so in VV channel, it shows a higher coherence value compared to the vegetation zones in the border. VH exhibits notably lower coherence in contrast to the VV due to its significantly smaller amplitude value within the dam area. Notably, the number of DS in the OPT is lower, but they exhibit higher coherence values (see Fig. 3(f)) than in VV channel. Most coherence range from 0.6 to 1 in OPT channel and 0.4 to 0.8 in VV channel. In the next section we will analyze the deformation results provided by DS points, which are influenced by the identified SHP groups and the associated coherence values.

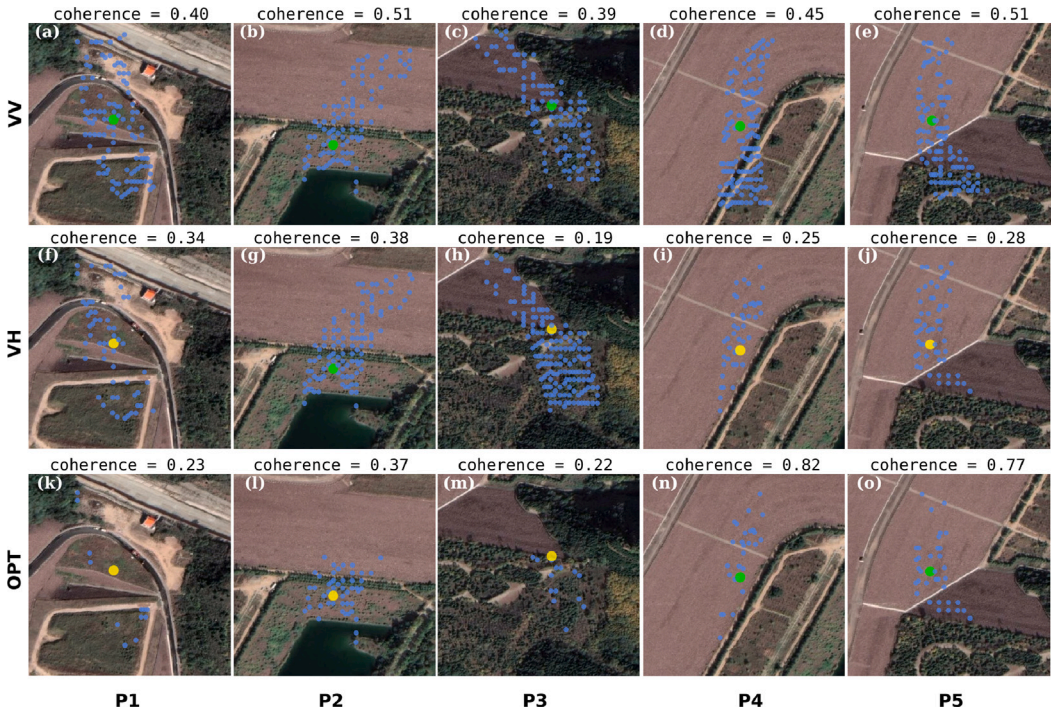

Fig. 5. SHP groups of five selected pixels (marked in Fig. 2) in Xiaolangdi Dam. Selected similar pixels are marked in blue, the reference pixel is shown as a large circle (DS in green, non-measurement point in yellow). (For interpretation of the references to color in this figure legend, the reader is referred to the web version of this article.)

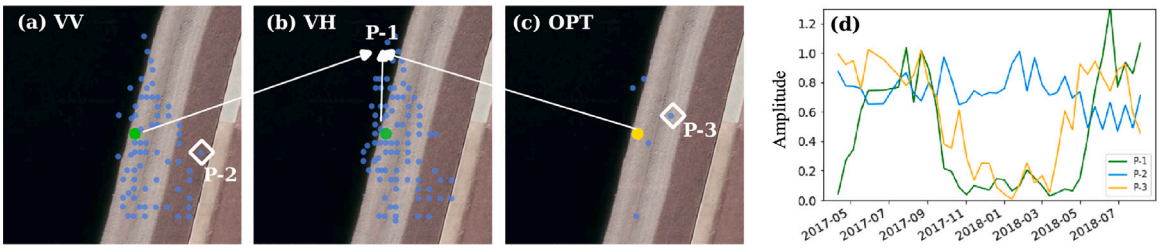

Fig. 6. SHP group of a single pixel (P6 marked in Fig. 2) adjacent to the water in Xiaolangdi Dam for (a) VV; (b) VH; (c) OPT. Selected similar pixels are marked in blue, the reference pixel is shown as a large circle (DS in green, non-measurement point in yellow). (d) Time series of the amplitude of VV at the pixels labeled as P-1, P-2, and P-3. (For interpretation of the references to color in this figure legend, the reader is referred to the web version of this article.)

To analyze which ground targets contribute to the phase of DS points, the SHP groups of five selected pixels are shown in Fig. 5. For the first three pixels in each channel, the central (or reference) pixel is located within an area of short vegetation. It is observed that the VV and VH channels, when used alone, mix the vegetated area with the bare ground and rock areas. For VV, it results in an improved coherence value. Together with the large number of SHP points, these pixels were selected as DS in the VV channel but rejected in the OPT channel. The reason is that pixels in OPT channel show a more restricted SHP group, i.e., formed only by pixels within the short vegetation area. This results in final lower coherence values. The lower coherence values and smaller SHP groups in the OPT channel produce their rejection during the selection of these three pixels as DS points.

For the fourth and fifth cases, the central pixels are located on a bare ground area, and they are selected as DS in OPT and VV channels. Although VH identifies an accurate SHP map in Fig. 5(i)–(j), its low coherence prevents these points from being chosen as DS. It is observed that the coherence value in the OPT channel is higher than in the VV channel, as the VV channel still mixes bare ground with vegetation targets, resulting in lower coherence. Despite the lower number of similar pixels in the OPT channel, the higher coherence values of these pixels led to their selection as DS. Therefore, the conclusion from Fig. 5 is that the increase in the number of DS points provided by the VV alone is achieved at the price of mixing pixels which actually correspond to different land covers. The homogeneity of the SHP groups is better guaranteed by the dual-polarimetric data.

One interesting observation is that only VV and VH channel selects DS points on the left side of the dam wall, specifically in the white rock area, whereas the OPT channel does not select any pixel in this area. Fig. 6 shows the SHP group for one typical pixel in this area and the time series of the amplitude for the reference pixel and other two pixels of the SHP groups found with VV, VH and OPT channels.

It is evident that from June to September, the central pixel represents a rock target (higher amplitude), while from November to May, the central pixel (P-1) is located in the water (lower amplitude) as a result of the rise of the water level due to an increase in water storage. The pixel in the SHP group of OPT channel (P-3) shows a similar amplitude change pattern as P-1, but the pixel in the VV channel (P-2) has a different temporal behavior, since it is never covered by water. By analyzing the location of the SHP groups with the help of the optical images, it becomes clear that in VV and VH, many pixels in SHP group are located in the water during an important part of the year, but this kind of pixels is rejected to be a DS in OPT channel.

In the test area of Barcelona, similar mixtures of different land covers in the SHP group of VV and VH can also be observed, for instance in Fig. 7(a)–(e) and Fig. 7(g)–(j), respectively. A pixel located on the

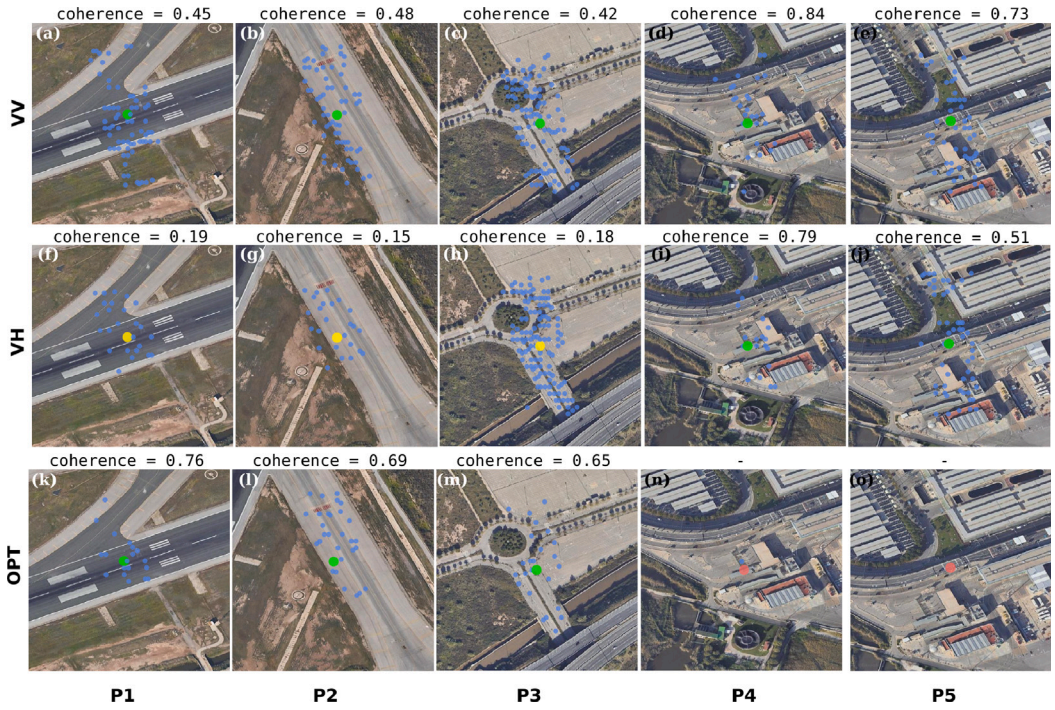

Fig. 7. SHP groups of five selected pixels (marked in Fig. 2) in Barcelona Airport. Selected similar pixels are marked in blue, the reference pixel is shown as a large circle (DS in green, PS in red, non-measurement in yellow). (For interpretation of the references to color in this figure legend, the reader is referred to the web version of this article.)

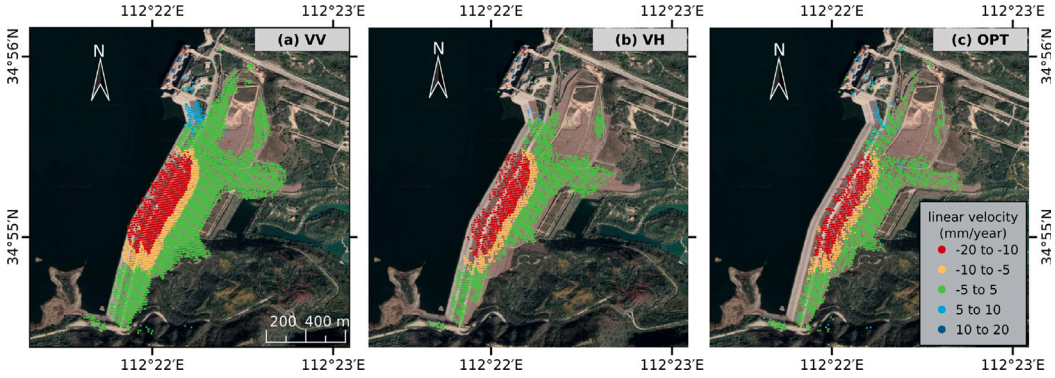

Fig. 8. Linear velocity map for VV, VH and OPT over Xiaolangdi Dam.

roof or road might be misinterpreted as a pixel on grassland by VV and VH channels. The OPT channel, utilizing polarization information, demonstrates better capability in distinguishing between vegetation and the road. These confusions can potentially affect the measurement results, considering that different land covers are expected to exhibit varying deformation rates, e.g. buildings have foundations but roads do not.

4.3. Analysis of the influence on deformation estimation

4.3.1. Results in Xiaolangdi Dam

By analyzing the velocity map in Fig. 8, it becomes evident that the deformation mainly occurs in the upper and middle sections of the dam. The large number of DS points detected by VV and VH channels contribute as additional measurement points to the existing deformation areas but do not reveal new deformation areas. In fact, the deformation measured over the white rock part of the dam (the wall closest to the water) is a mere replica of the deformation measured in the brown rock area. This result is an obvious consequence of the selection of SHP groups for the pixels in the white rock area, already discussed in the previous section. The deformation estimation over these pixels is really based on the higher quality pixels in the brown rock area, which is never covered by water. Therefore, the deformation measurement obtained by the VV and VH over that part of the dam is not reliable. In addition, the PS points detected in the OPT channel show the ability to detect a new deformation area located at the top of the dam, which is not visible in the result of VV or VH.

To further compare the deformation obtained by the VV, VH and OPT channels, a transect or fold line was defined along the dam, as depicted in Fig. 9. The yellow fold line spans approximately 1500 m, passing through the front of the dam. To calculate the average velocity along the line, all measurement points within a 10 m buffer of the fold line were selected. When considering the deformation measured by the PS points alone, it becomes clear that the OPT channel reveals some deformation concentrated in a small area (e.g. at 200 m) and provide measurement points, e.g. at positions around 300 m and 1000 m, in which VV or VH fails to detect any PS point. The difference between VV, VH and OPT channels is also reflected in the deformation values

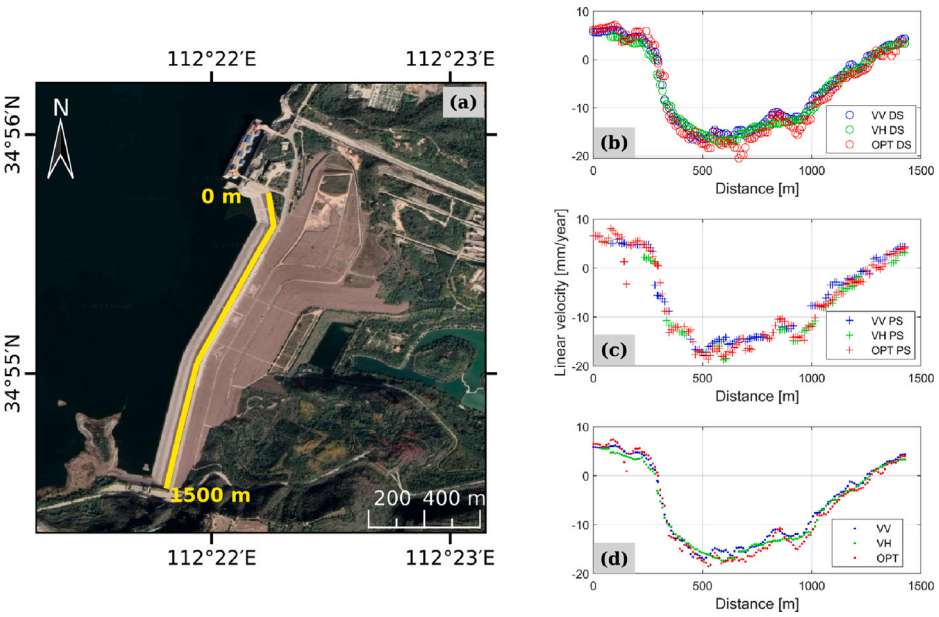

Fig. 9. Deformation rate along a fold line (marked as yellow line) over Xiaolangdi dam. The linear velocity was calculated as the mean value of the PS, DS or ALL (PS and DS) measurement points within a 10 m buffer of the fold line. (For interpretation of the references to color in this figure legend, the reader is referred to the web version of this article.)

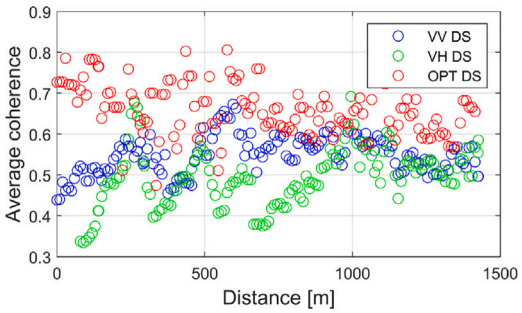

Fig. 10. Average coherence for DS along a fold line over Xiaolangdi Dam, calculated as the average of the DS within a 10 m buffer of the fold line. The number of DS in VV, VH and OPT channel is 483, 312 and 169.

provided at the DS points. The average deformation rate obtained from the OPT is larger than that of the VV and VH at most positions along the transect. He et al. (2022) used in-situ data as a reference to verify the deformation at the dam center is 20–25 mm/year between March 2017 and October 2020. The center of the dam corresponds to the range of 500–800 m in Fig. 9. It is evident that the result obtained from the OPT is closer to this value. This proves that the large number of SHP points identified by the VV and VH leads to a loss of deformation details. The spatial averaging blurs the deformation phase gradients, resulting in a decrease in deformation details.

The incorporation of the VH in OPT channel results in a higher number of PS points. The number of PS in VV, VH and OPT channel is 93, 44 and 165, respectively. In terms of DS, the average coherence for DS points around the fold line is shown in Fig. 10. It is evident that the advantage of using polarimetric information consists of detecting higher quality DS points, i.e., with higher coherence values, and of keeping the original deformation pattern by avoiding mixing pixels from heterogeneous areas.

4.3.2. Results in Barcelona Airport

The linear velocity map over the whole Barcelona Airport is depicted in Fig. 11, and two specific areas within the airport are zoomed in and displayed in Fig. 12. In these images, the white-background pixels are classified as DS in the VV channel but as PS in the OPT channel. The PS points obtained from the OPT Fig. 11(c,f) exhibit similar deformation patterns as reported in other studies (Iglesias et al., 2014; Navarro-Sanchez and Lopez-Sanchez, 2014). However, the deformation rates at the DS points in VV and VH are lower compared to the OPT. This is because the DS in VV and VH include different land covers with varying velocities, as illustrated in Fig. 7.

5. Discussion

PolPSI studies with DS have been focused on the selection criterion and on the number of measurement points reached in comparison with single-polarimetric data.

Researchers have employed statistical tests such as KS and GLR to analyze and compare single- and multi-polarimetric data, as utilized by Navarro-Sanchez and Lopez-Sanchez (2014). Their findings revealed interesting aspects when comparing the number of DS detected using different channels. For example, in a test site in Barcelona city with Radarsat−2 data, the number of DS identified through polarimetry was lower than that using only the HH channel. Conversely, in a test site in Murcia city using TerraSAR−X data, the number of DS was lower in the HH channel than with dual-pol HH and VV data. This discrepancy was attributed to the spatial resolution of the images. The high resolution of TerraSAR−X (pixel dimension 2.44 m × 0.91 m) allows for the collection of sufficient pixels with single scattering mechanisms, thus meeting the criteria for being DS. However, the pixels in images with coarser resolution, for example Radarsat−2 (5.1 m × 4.7 m) and S1 (13.9 m × 2.33 m), may be already composed of different scattering features. This imposes higher requirements on potential ground objects that can be identified with good quality and also restricts the number of pixels available in an area of fixed size. Furthermore, the incorporation of full polarization information (as in Radarsat−2) makes more demanding the task of identifying enough similar pixels, resulting in a large reduction in the number of DS.

In the study by Zhao et al. (2022), dual-pol S1 data were used, and the SHP detection was based on the FaSHPS method (Jiang et al., 2015). However, FaSHPS only works on amplitude images. Therefore,

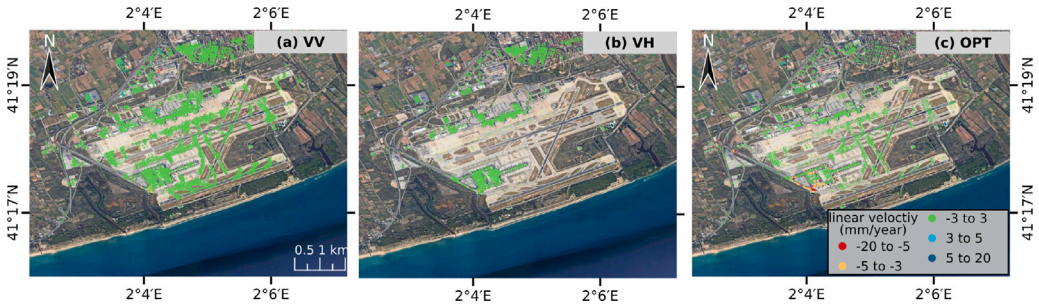

Fig. 11. Linear velocity map for VV, VH and OPT over Barcelona Airport.

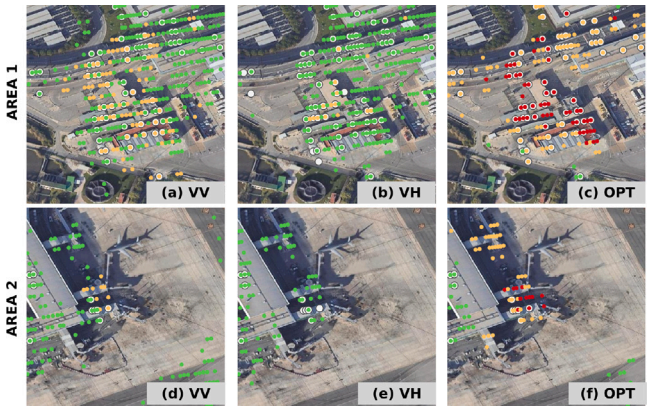

Fig. 12. Two areas of the Barcelona airport show different deformation results in the VV, VH and OPT channels (marked in Fig. 2). White circles indicate measurement points classified as DS in VV but as PS in OPT. Green points represent stable points with a linear velocity of −3 to 3 mm/year, while orange and rend points represent points with a velocity of −5 to −3 mm/year and −20 to −5 mm/year, respectively. (For interpretation of the references to color in this figure legend, the reader is referred to the web version of this article.)

the SHP set was detected separately by inspecting the VV and VH amplitudes, instead of using a polarimetric covariance matrix. The final SHP group of dual-polarimetric data was the combination of the VV and VH groups, thus more DS were selected in dual-polarimetric data than in any of the two individual channels. In that work the Xiaolangdi dam was also employed as a test site, and interestingly, the pixels near the left side of the dam (white rock area) were also selected as DS. Since they were selected on the basis of the information contained in the separate polarization channels (VV and VH), not jointly using that information, the result is equivalent to the one obtained in our work when using only the VV channel. As we have demonstrated in this work with a more detailed analysis, these points are located in the water during an important part of the year, so they should not be selected for deformation measurement. If they are selected, the estimated deformation just replicates the values measured in the adjacent areas.

In Mullissa et al. (2017, 2018), Zhao and Mallorqui (2019b), a different approach was employed to select the similar pixels that form the SHP groups when data are polarimetric. The approach is based on their scattering properties using decomposition methods. The results demonstrated that the inclusion of multi-polarimetric channels increased the number of both PS and DS. In Mullissa et al. (2017), it was observed that the deformation results derived from DS differed from the results obtained from nearby PS. Furthermore, as the number of DS increased, the corresponding deformation rates for individual pixels became smaller. This phenomenon was attributed to potential unwrapping errors in that article. However, a more detailed analysis of this phenomenon could be conducted by examining the homogeneity of the SHP group for each pixel.

In our experiments, the pixels forming each SHP group were identified by their statistical properties using the GLR test for both single- and dual-polarimetric cases. As observed in the experiments conducted on Xiaolangdi Dam and Barcelona Airport, the introduction of the VH channel leads to a substantial decrease in the number of DS and an increase in the number of PS. However, when using the VV or VH alone, the DS often include various scattering mechanisms (i.e., different land covers) in the corresponding SHP groups. It is important to clarify that this confusion primarily arises from the lack of polarization information rather than the threshold used in the GLR test. In the Results section, we employed the same false alarm rate for both the VV, VH and OPT channels. In this section, we aim to illustrate this issue by tightening the threshold for the VV channel in Fig. 13, so the selection of pixels in that case becomes stricter than in the previous results. We selected the VV for comparison because, when using S1 data for deformation monitoring, the VH is usually discarded due to its lower amplitude. The experiment detailed in this paper further confirms that the VH channel yields fewer measurement points compared to the VV channel.

It is clear in Fig. 13(i)–(k) that even with a stricter threshold, the mixing of different land covers still exists. Furthermore, when setting a threshold that yields a comparable number of SHP around the dam as the OPT channel (Fig. 13(m)–(o)), the pixels located at the vegetation and rock boundary remain confused. With this modified threshold, the identified SHP points fail to meet the filtering requirements for subsequent PSI processing.

An important consideration arises concerning how to deal with the trade-off between spatial coverage and accuracy of measurement points, since the introduction of polarimetric information leads to a decrease in the total measurement points but they are more reliable than the obtained with single-pol data. In scenarios primarily involving artificial structures, the PS provided by OPT channel are sufficient to reveal the same or even more deformation areas compared with the VV channel. When the study site is located at a natural area, the final user needs to state what is the preferred result: a more reliable one with areas not covered by measurement points, or an (almost) fully-covered product in which many of the values are known to be not reliable. Since the threshold selection is not a solution to get the desired trade-off, more advanced techniques for DSI, as those envisaged in Mullissa et al. (2018), Shen et al. (2022a), could contribute to this purpose.

6. Conclusions

In this study, we have analyzed the impact of using PolPSI with S1 data on distributed scatterers. The experiments carried out have

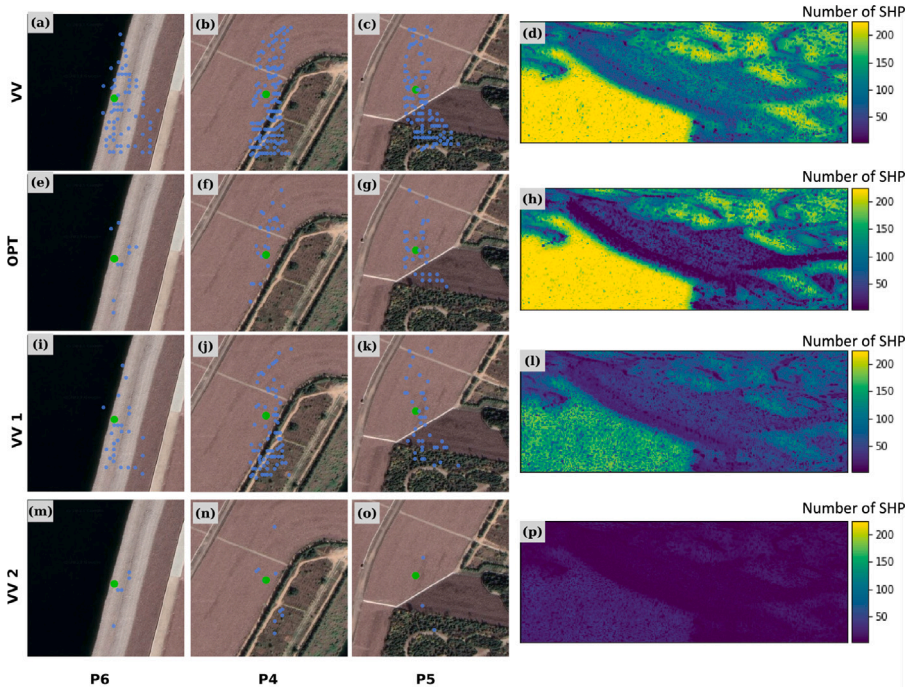

Fig. 13. Results obtained with different thresholds over Xiaolangdi Dam. VV and OPT denote selection with a 5% false alarm rate. VV 1 and VV 2 denote selections carried out using a tighter threshold and an extremely tight threshold R_{thr} in (12). The first three lines represent SHP groups for selected pixels (marked in Fig. 2), and the last line shows the number of SHP for the whole research area. The color bar represents the number of SHP for each pixel within the search window 15 × 15.

provided answers to the questions raised in the Introduction section, as follows:

1. *What is the contribution of using dual-polarimetric data in the SHP group identification, from the point of view of the scene properties?* By incorporating the VH channel, a more stringent selection of SHP is achieved. This is achieved by using the polarimetric covariance matrix to characterize each individual pixel, not the two channels independently. Pixels which exhibit different scattering properties compared to the reference pixel are not considered as SHP. Additionally, pixels representing different behavior in the temporal dimension are also excluded.
2. *Is there a quantitative improvement in PSI results in terms of number of DS and/or quality of the estimated deformation?* It has been observed that the improvement in DS is in terms of quality rather than quantity. Compared with the deformation results in VV or VH alone, these enhanced DS points offer similar deformation areas with reduced coverage, but providing more reliable deformation details.
3. *Is it worth to use always the VH channel, in addition to VV, or is it better to work with the VV channel alone?* If the focus is on obtaining accurate and reliable measurement results for an area of interest, it is recommended to use the OPT channel. Otherwise, the larger number of measurement points and wider coverage provided the VV channel may include unreliable measurements characterized by points with replicated deformation values (i.e. extracted from other points) or blurred estimates which suffer from a lack of spatial detail or more extreme deformation values.

In summary, despite the appealing aspect of the results obtained by the VV channel alone, characterized by an extended spatial coverage with a large amount of measurement points, it is important to be cautious about the values measured at the DS, since they may represent replicas from other nearby pixels or mixtures of different land covers. Instead, the dual-polarimetric results are clearly more reliable, because they avoid fake DS detected in the VV channel. The use of more advanced techniques especially designed for polarimetric DSI, such as those proposed by Mullissa et al. (2018) or Shen et al. (2022a), could provide better final results in the dual-pol case, e.g. by increasing the number of final DS after processing the data with specific tools.

CRediT authorship contribution statement

Jiayin Luo: Conceptualization, Methodology, Software, Visualization, Data curation, Investigation. **Juan M. Lopez-Sanchez:** Supervision, Software, Writing – review & editing. **Francesco De Zan:** Conceptualization, Supervision.

Declaration of competing interest

The authors declare that they have no known competing financial interests or personal relationships that could have appeared to influence the work reported in this paper.

Data availability

The authors do not have permission to share data.

References

Berardino, P., et al., 2002. A new algorithm for surface deformation monitoring based on small baseline differential SAR interferograms. IEEE Trans. Geosci. Remote Sens. 40 (11), 2375–2383. http://dx.doi.org/10.1109/TGRS.2002.803792.

Blanco-Sanchez, P., et al., 2009. The coherent pixels technique (CPT): An advanced DInSAR technique for nonlinear deformation monitoring. Pure Appl. Geophys. 165, 1167–1193. http://dx.doi.org/10.1007/978-3-7643-8907-9_10.

Cloude, S., Papathanassiou, K., 1998. Polarimetric SAR interferometry. IEEE Trans. Geosci. Remote Sens. 36 (5), 1551–1565. http://dx.doi.org/10.1109/36.718859.

Conradsen, K., et al., 2003. A test statistic in the complex Wishart distribution and its application to change detection in polarimetric SAR data. IEEE Trans. Geosci. Remote Sens. 41 (1), 4–19. http://dx.doi.org/10.1109/TGRS.2002.808066.

Deledalle, C.A., et al., 2015. NL-SAR: A unified nonlocal framework for resolution-preserving (Pol)(In)SAR denoising. IEEE Trans. Geosci. Remote Sens. 53 (4), 2021–2038. http://dx.doi.org/10.1109/TGRS.2014.2352555.

Dong, J., et al., 2018. A unified approach of multitemporal SAR data filtering through adaptive estimation of complex covariance matrix. IEEE Trans. Geosci. Remote Sens. 56 (9), 5320–5333. http://dx.doi.org/10.1109/TGRS.2018.2813758.

Dong, J., et al., 2021. Multi-scale deformation monitoring with Sentinel-1 InSAR analyses along the middle route of the south-north water diversion project in China. Int. J. Appl. Earth Obs. Geoinformation 100, 102324. http://dx.doi.org/10.1016/j.jag.2021.102324.

Ferretti, A., et al., 2000. Nonlinear subsidence rate estimation using permanent scatterers in differential SAR interferometry. IEEE Trans. Geosci. Remote Sens. 38 (5), 2202–2212. http://dx.doi.org/10.1109/36.868878.

Ferretti, A., et al., 2001. Permanent scatterers in SAR interferometry. IEEE Trans. Geosci. Remote Sens. 39 (1), 8–20. http://dx.doi.org/10.1109/36.898661.

Ferretti, A., et al., 2011. A new algorithm for processing interferometric data-stacks: SqueeSAR. IEEE Trans. Geosci. Remote Sens. 49 (9), 3460–3470. http://dx.doi.org/10.1109/TGRS.2011.2124465.

Goodman, N.R., 1963. Statistical analysis based on a certain multivariate complex Gaussian distribution (An Introduction). Ann. Math. Stat. 34 (1), 152–177, URL: http://www.jstor.org/stable/2991290.

Hagberg, J.O., et al., 1995. Repeat-pass SAR interferometry over forested terrain. IEEE Trans. Geosci. Remote Sens. 33 (2), 331–340. http://dx.doi.org/10.1109/TGRS.1995.8746014.

He, Z., et al., 2022. Deformation monitoring of xiaolangdi dam based on SBAS-InSAR technology. Sci. Surv. mapp. 47 (5), 66–72. http://dx.doi.org/10.16251/j.cnki.1009-2307.2022.05.009.

Hooper, A., et al., 2004. A new method for measuring deformation on volcanoes and other natural terrains using InSAR persistent scatterers. Geophys. Res. Lett. 31, 1–5. http://dx.doi.org/10.1029/2004GL021737.

Hooper, A., et al., 2007. Persistent scatterer interferometric synthetic aperture radar for crustal deformation analysis, with application to Volcan Alcedo, Galapagos. J. Geophys. Res.: Solid Earth 112 (B7), http://dx.doi.org/10.1029/2006JB004763.

Iglesias, R., et al., 2014. Phase quality optimization in polarimetric differential SAR interferometry. IEEE Trans. Geosci. Remote Sens. 52 (5), 2875–2888. http://dx.doi.org/10.1109/TGRS.2013.2267095.

Iglesias, R., et al., 2015. Polarimetric optimization of temporal sublook coherence for DInSAR applications. IEEE Geosci. Remote Sens. Lett. 12 (1), 87–91. http://dx.doi.org/10.1109/LGRS.2014.2326684.

Jiang, M., et al., 2015. Fast statistically homogeneous pixel selection for covariance matrix estimation for multitemporal InSAR. IEEE Trans. Geosci. Remote Sens. 53 (3), 1213–1224. http://dx.doi.org/10.1109/TGRS.2014.2336237.

Lee, J.S., et al., 1994. Intensity and phase statistics of multilook polarimetric and interferometric SAR imagery. IEEE Trans. Geosci. Remote Sens. 32 (5), 1017–1028. http://dx.doi.org/10.1109/36.312890.

Liu, Y., et al., 2021. Monitoring of surface deformation in a low coherence area using distributed scatterers InSAR: Case study in the Xiaolangdi basin of the Yellow River, China. Bull. Eng. Geol. Environ. 80, 25–39. http://dx.doi.org/10.1007/s10064-020-01929-1.

Luo, J., et al., 2022. Assessment of the contribution of polarimetric persistent scatterer interferometry on Sentinel-1 data. IEEE J. Sel. Top. Appl. Earth Obs. Remote Sens. 15, 7997–8009. http://dx.doi.org/10.1109/JSTARS.2022.3206550.

Luo, J., et al., 2023. Despeckling multi-temporal polarimetric SAR data based on tensor decomposition. IEEE J. Sel. Top. Appl. Earth Obs. Remote Sens. 16, 1–16. http://dx.doi.org/10.1109/JSTARS.2023.3266823.

Monserrat, O., et al., 2011. The thermal expansion component of persistent scatterer interferometry observations. IEEE Geosci. Remote Sens. Lett. 8 (5), 864–868. http://dx.doi.org/10.1109/LGRS.2011.2119463.

Mora, O., et al., 2003. Linear and nonlinear terrain deformation maps from a reduced set of interferometric SAR images. IEEE Trans. Geosci. Remote Sens. 41 (10), 2243–2253. http://dx.doi.org/10.1109/TGRS.2003.814657.

Mullissa, A.G., et al., 2017. Polarimetric differential SAR interferometry in an arid natural environment. Int. J. Appl. Earth Obs. Geoinformation 59, 9–18. http://dx.doi.org/10.1016/j.jag.2017.02.019.

Mullissa, A.G., et al., 2018. Polarimetry-based distributed scatterer processing method for PSI applications. IEEE Trans. Geosci. Remote Sens. 56, 3371–3382. http://dx.doi.org/10.1109/TGRS.2018.2798705.

Murdaca, G., et al., 2022. Deep learning for InSAR phase filtering: An optimized framework for phase unwrapping. Remote Sens. 14 (19), 4956. http://dx.doi.org/10.3390/rs14194956.

Navarro-Sanchez, V.D., Lopez-Sanchez, J.M., 2012. Improvement of persistent-scatterer interferometry performance by means of a polarimetric optimization. IEEE Geosci. Remote Sens. Lett. 9 (4), 609–613. http://dx.doi.org/10.1109/LGRS.2011.2176715.

Navarro-Sanchez, V.D., Lopez-Sanchez, J.M., 2014. Spatial adaptive speckle filtering driven by temporal polarimetric statistics and its application to PSI. IEEE Trans. Geosci. Remote Sens. 52 (8), 4548–4557. http://dx.doi.org/10.1109/TGRS.2013.2282406.

Navarro-Sanchez, V.D., et al., 2010. A contribution of polarimetry to satellite differential SAR interferometry: Increasing the number of pixel candidates. IEEE Geosci. Remote Sens. Lett. 7 (2), 276–280. http://dx.doi.org/10.1109/LGRS.2009.2033013.

Neumann, M., et al., 2008. Multibaseline polarimetric SAR interferometry coherence optimization. IEEE Geosci. Remote Sens. Lett. 5 (1), 93–97. http://dx.doi.org/10.1109/LGRS.2007.908885.

Parizzi, A., Brcic, R., 2011. Adaptive InSAR stack multilooking exploiting amplitude statistics: A comparison between different techniques and practical results. IEEE Geosci. Remote Sens. Lett. 8 (3), 441–445. http://dx.doi.org/10.1109/LGRS.2010.2083631.

Pipia, L., et al., 2009. Polarimetric differential SAR interferometry: First results with ground-based measurements. IEEE Geosci. Remote Sens. Lett. 6 (1), 167–171. http://dx.doi.org/10.1109/LGRS.2008.2009007.

Rosi, A., et al., 2016. Subsidence mapping at regional scale using persistent scatters interferometry (PSI): The case of Tuscany region (Italy). Int. J. Appl. Earth Obs. Geoinformation 52, 328–337. http://dx.doi.org/10.1016/j.jag.2016.07.003.

Shen, P., et al., 2022a. JPPL: A joint-polarization phase linking algorithm for phase optimization of TSPolInSAR data. Int. J. Appl. Earth Obs. Geoinformation 112, 102889. http://dx.doi.org/10.1016/j.jag.2022.102889.

Shen, P., et al., 2022b. A polarization stacking method for optimizing time-series interferometric phases of distributed scatterers. Remote Sens. 14 (17), http://dx.doi.org/10.3390/rs14174168.

Sica, F., et al., 2018. InSAR-BM3D: A nonlocal filter for SAR interferometric phase restoration. IEEE Trans. Geosci. Remote Sens. 56 (6), 3456–3467. http://dx.doi.org/10.1109/TGRS.2018.2800087.

Sica, F., et al., 2021. Φ-Net: Deep residual learning for InSAR parameters estimation. IEEE Trans. Geosci. Remote Sens. 59 (5), 3917–3941. http://dx.doi.org/10.1109/TGRS.2020.3020427.

Stephens, M.A., 1970. Use of the Kolmogorov-Smirnov, Cramer-Von Mises and related statistics without extensive tables. J. R. Stat. Soc. 32 (1), 115–122.

Wang, Y., et al., 2023. Automatic detection and update of landslide inventory before and after impoundments at the Lianghekou reservoir using Sentinel-1 InSAR. Int. J. Appl. Earth Obs. Geoinformation 118, 103224. http://dx.doi.org/10.1016/j.jag.2023.103224.

Wu, B., et al., 2015. New methods in multibaseline polarimetric SAR interferometry coherence optimization. IEEE Geosci. Remote Sens. Lett. 12 (10), 2016–2020. http://dx.doi.org/10.1109/LGRS.2015.2443000.

Wu, B., et al., 2016. Improved SNR optimum method in PolDInSAR coherence optimization. IEEE Geosci. Remote Sens. Lett. 13 (7), 982–986. http://dx.doi.org/10.1109/LGRS.2016.2557485.

Zhao, F., Mallorqui, J.J., 2019a. Coherency matrix decomposition-based polarimetric persistent scatterer interferometry. IEEE Trans. Geosci. Remote Sens. 57 (10), 7819–7831. http://dx.doi.org/10.1109/TGRS.2019.2916649.

Zhao, F., Mallorqui, J.J., 2019b. SMF-POLOPT: An adaptive multitemporal Pol(DIn)SAR filtering and phase optimization algorithm for PSI applications. IEEE Trans. Geosci. Remote Sens. 57 (9), 7135–7147. http://dx.doi.org/10.1109/TGRS.2019.2911670.

Zhao, F., et al., 2022. Polarimetric persistent scatterer interferometry for ground deformation monitoring with VV-VH Sentinel-1 data. Remote Sens. 14 (2), http://dx.doi.org/10.3390/rs14020309.

Zhao, F., et al., 2023. An efficient polarimetric persistent scatterer interferometry algorithm for dual-pol Sentinel-1 data. IEEE J. Sel. Top. Appl. Earth Obs. Remote Sens. 16, 3336–3352. http://dx.doi.org/10.1109/JSTARS.2023.3260850.